Figure 1. Joint distribution of moment-derived line-of-sight velocity dispersion and mean velocity. The thermal, instrumental, and fine-structure contributions to the velocity dispersion have been subtracted in quadrature. Mean velocities are shown with respect to the systemic velocity of the stellar cluster ($+7$ km s^{-1} in the Local Standard of Rest frame, or $+25$ km s^{-1} in the Heliocentric frame, Tobin et al. 2009).

3 RESULTS

### 3.3 Plane-of-sky versus line-of-sight velocity variations

The non-thermal line-of-sight velocity dispersion $\sigma_{\rm los}$ may be estimated by correcting the observed line widths for the contributions from the spectrograph resolution, fine-structure splitting, and thermal Doppler broadening, as in Eq. (2) of García-Díaz et al. (2008). A striking fact about the nebular line profiles is that the line-of-sight velocity dispersion is several times larger than the plane-of-sky dispersion in mean velocities. This is illustrated in Figure 1, which shows flux-weighted histograms of the non-thermal RMS line widths versus mean velocity for all lines of the García-Díaz et al. (2008) spectral axis. The line-of-sight RMS velocity dispersion is 9–10 km s^{-1}, whereas the RMS plane-of-sky dispersion of the mean velocities is only 2–4 km s^{-1}.

However, the observed line widths are affected by additional broadening due to dust-scattering (Castañeda 1988; Henney 1998), which gives an extended red wing to the line profile that contains 10–20% of the total line flux (see Fig. 2). By means of fitting multiple Gaussian components to each line profile, it is possible to effectively remove this scattered component and calculate statistics for the line core alone. We have done this for the [O III] line, with results shown in the inset box of Figure 2. It can be seen that the line-of-sight velocity dispersion is reduced by almost a factor of two.

It is more difficult to perform the Gaussian decomposition for the lower ionization lines since the back-scattered component is not as cleanly separated from the core component. On the other hand, an alternative method of suppressing the effects of scattering on the line widths is to use the Full Width at Half Maximum (FWHM) instead of the RMS width. Even a weak component with a velocity that is very different from the line centroid can have a
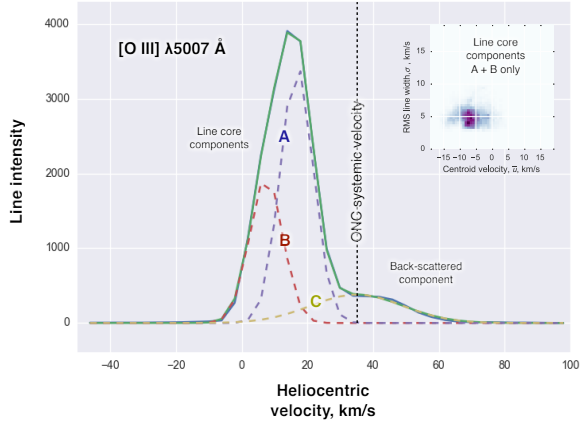
Figure 2. Typical [O III] line proile, showing Gaussian decomposition into three components, following the labeling of Castañeda (1988). The redshifted component C is due to back-scattering of the blue-shifted components A and B by dust that lies behind the emitting gas. Inset figure is same as Fig. 1, but after removing Component C from the profile.
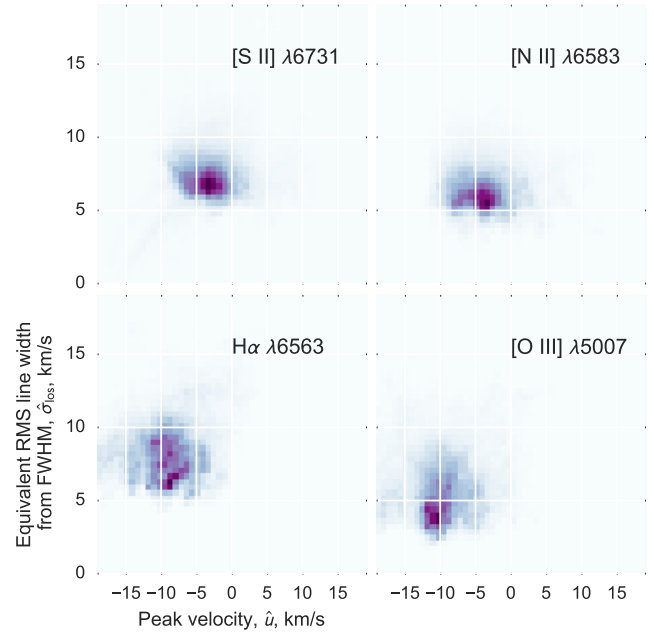
Figure 3. Same as Fig. 1 but substituting the FWHM-derived line width $\hat{\sigma}_{\rm los}$ for the moment-derived line width $\sigma_{\rm los}$ and substituting the peak velocity $\hat{u}$ for the mean velocity $\bar{u}$.

large effect on the $\sigma_{\rm los}$ due to the $(u - \bar{u})^2$ dependence of the second velocity moment. But the same component will have almost no effect on the FWHM if its amplitude is less than half that of the line core. We therefore define a FWHM-based effective σ as $\hat{\sigma}_{\rm los} = {\rm FWHM}/\sqrt{8\ln 2} \approx {\rm FWHM}/2.355$, with the constant of proportionality being chosen so that $\hat{\sigma}_{\rm los} = \sigma_{\rm los}$ for a Gaussian profile. The results are shown in Figure 3, where it can be seen that nearly all the lines show substantial reductions in the line-of-sight line widths with respect to the moment-derived values of Figure 1. The exception is Hα, where larger thermal broadening means that $\hat{\sigma}_{\rm los}$ is still contaminated by the back-scattered component due to blending. Note that $\hat{\sigma}_{\rm los}$ is insensitive to not only the scattered com-

(a)

(b)
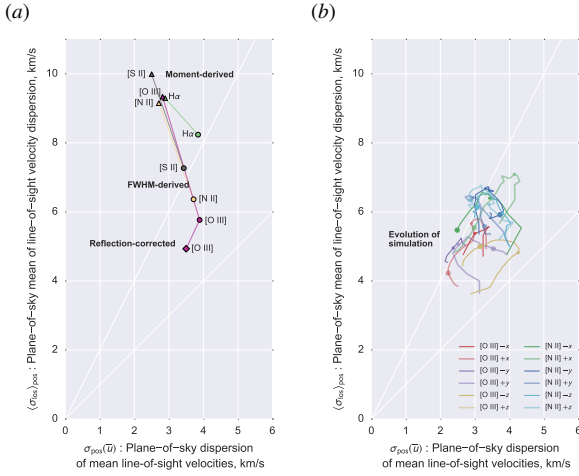
Figure 4. (a) Observational comparison of mean line-of-sight velocity dispersion (vertical axis) with plane-of-sky dispersion of mean line-of-sight velocity (horizontal axis). All averages were performed with flux weighting. Triangle symbols show the moment-derived values, which are contaminated by the back-scattered component. Circle symbols show the more robust FWHM-derived values, while the diamond symbol shows the reflection-corrected result from multi-Gaussian fitting, which was only possible for [O III]. The diagonal white lines show the relationships $\sigma_{\rm los} = \sigma_{\rm pos}$ and $\sigma_{\rm los} = 2\sigma_{\rm pos}$. (b) The same quantities derived from evolutionary tracks of the turbulent H II region simulation described in Medina et al. (2014) for different viewing directions as shown in the key: blue/green lines are for [N II], while red/purple/yellow lines are for [O III]. Evolutionary times of 0.15 Myr (small dot) and 0.25 Myr (larger dot) are marked on each track, and only those times where the mean line velocity is blueshifted are shown.

ponent, but also to any other weak component that is not blended with the line core. For the low-ionization lines such as [N II] and [S II], this includes the kinematic component known as the Diffuse Blue Layer (Deharveng 1973), which produces line splitting in the SE and N regions of our observed maps.

4 DISCUSSION

4.3 Turbulent contribution to spectral line broadening

So far we have concentrated on the slopes of the structure function and power spectra, since they can be theoretically related to the spectrum of underlying velocity fluctuations in the nebula. However, other questions require consideration of the magnitude of the velocity fluctuations, as measured by different techniques. Such questions include whether turbulence alone is sufficient to account for the non-thermal line broadening observed in the nebula, and whether that turbulence is driven primarily by the large scale thermal expansion of the nebula, or by smaller scale photoevaporation flows, and to what extent stellar winds play a role.

The plane-of-sky dispersion in centroid velocities $\sigma_{\rm pos}(\bar{u})$ is the RMS width of the marginal distribution along the $\bar{u}$ axis of Figure 1, which is the same as the quantity $\sigma_{\rm vc}$ used to normalize the structure functions in § 2. Figure 4(a) summarizes the observational determination of $\sigma_{\rm los}$ and $\sigma_{\rm pos}$, while Figure 4(b) shows the same quantities calculated for the turbulent H II region simulation of Medina et al. (2014), as presented in the Appendix. As discussed in § 3.3, the FWHM-derived and reflection-corrected observational values are the most reliable, and these fall broadly in
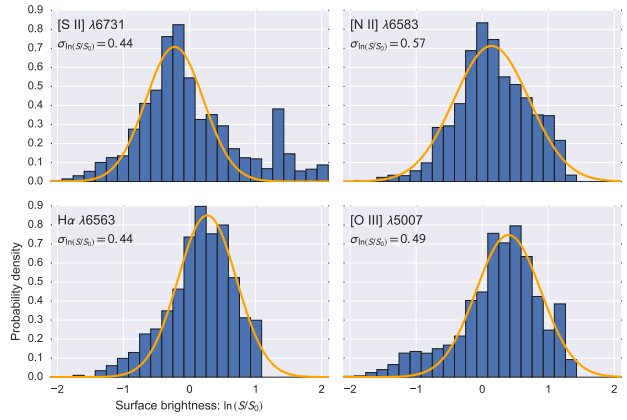
Figure 5. Probability density functions (PDF, blue histograms) of observed surface brightness maps in different emission lines after binning 16×16 pixels to eliminate small scale variations. The surface brightness is normalized by the mean value and shown on a natural logarithmic scale, and the PDFs are weighted by the surface brightness itself. A log-normal distribution (orange lines) is fitted to the core of each PDF (only the part of the histogram with probability density > 0.3 times the maximum). The fitted RMS width σ of the log-normal distribution is indicated on each panel.

the same region of the graph as do the evolutionary tracks, with $\sigma_{\rm pos} \approx 3 \pm 1$ km s^{-1} and $\sigma_{\rm los} \approx 6 \pm 1$ km s^{-1}.

The fact that the line-of-sight velocity dispersion is roughly twice the plane-of-sky velocity dispersion can be interpreted in at least two different ways. In the case of a homogeneous turbulent velocity field with characteristic correlation length l_0, the projection from three to two dimensions over a line-of-sight depth L reduces the plane-of-sky amplitude of fluctuations if $l_0 < L$, a phenomenon known as "projection smearing" (von Hoerner 1951; Scalo 1984). Our l_0 and $\sigma_{\rm pos}/\sigma_{\rm los}$ correspond to s_0 and $\sigma_{\rm obs}/\sigma_{\rm true}$ in Fig. 1 of Scalo (1984), from which it can be seen that a value of 0.5 requires $l_0/L \approx 0.02$–0.1, depending on the steepness of the velocity fluctuation spectrum. The results from our structure function analysis (§ **??**) imply a correlation length $l_0 \approx 0.1$–0.2 pc for all lines, which would require a very large line-of-sight depth $L > 1$ pc in order to explain the observed $\sigma_{\rm pos}/\sigma_{\rm los}$ by projection smoothing. This is wildly inconsistent with independent evidence (Baldwin et al. 1991; O'Dell 2001; García-Díaz & Henney 2007) that the emitting layer thickness is much smaller than this in the region covered by our maps: $L \approx 0.01$–0.3 pc, being thinner on the West side and for the lower ionization lines.

The same discrepancy arises when the projection smearing argument is applied to our simulated H II region. In this case, $l_0 \approx 0.5$–1 pc for evolutionary times later than 0.15 Myr (Fig. A4 of Medina et al. 2014), thus requiring $L > 5$ pc, which is clearly unacceptable since it is bigger than the computational box of the simulation. For both the simulation and the observations, it is clear that $l_0 \approx L$ for the high-ionization lines and $l_0 > L$ for the low-ionization lines. Therefore, projection smearing of the large-scale fluctuations is negligible and cannot explain the difference between $\sigma_{\rm pos}$ and $\sigma_{\rm los}$.

A second, contrasting interpretation of the evidence would be in terms of large-scale, ordered motions. Consider an emission shell that expands at velocity v. If the shell emissivity is homogeneous, then the integrated line profile is rectangular, with mean velocity $\bar{u} = 0$ and velocity width $\sigma_{\rm los} = v/2$. Furthermore, the spatially resolved line profile at any point will also have $\bar{u} = 0$, so that

$\sigma_{\text{pos}} = 0$. However, if there are emissivity fluctuations between different parts of the shell, then $\bar{u}$ will fluctuate on the plane of the sky, according to the relative brightness of the red-shifted and blue-shifted hemispheres. The required RMS fractional variation in the emissivity on the scale of the shell diameter is found to be $\sigma_{E/E_0} \approx \sigma_{\text{pos}}/\sigma_{\text{los}}$.

The observed large-scale ($> 9''$) brightness fluctuations are illustrated in Figure 5, which shows log-normal fits to the PDFs of surface brightness, S, after normalizing by the mean, S_0, and binning the maps at 16×16 pixels. The RMS width of the log-normal PDF, $\sigma_{\ln S/S_0}$ is seen to be in the range 0.45–0.6 for all lines. This is related to the RMS fractional brightness fluctuation as $\sigma_{\ln S/S_0}^2 = \ln(1 + \sigma_{S/S_0}^2)$, or $\sigma_{\ln S/S_0} \approx \sigma_{S/S_0}$ if $\sigma_{S/S_0} < 1$. The relationship between σ_{E/E_0} and σ_{S/S_0} depends on both line-of-sight projection (Brunt et al. 2010), which tends to make $\sigma_{S/S_0} < \sigma_{E/E_0}$, and fluctuations in the foreground dust extinction, which have the opposite effect of increasing σ_{S/S_0}. We assume that the two effects roughly cancel, so that the surface brightness PDFs imply $\sigma_{E/E_0} \approx \sigma_{S/S_0} \approx 0.5$. This is equal to the value derived in the previous paragraph to be required by the observed $\sigma_{\text{pos}}/\sigma_{\text{los}}$, which implies that emissivity fluctuations combined with an ordered velocity field are entirely sufficient to explain the observed plane-of-sky variation in mean velocities, without requiring any fluctuations in the velocity field itself.

Although it is a priori unlikely that there are *no* velocity fluctuations in the ionized gas, this is yet another reason why the structure function of the mean velocity is not an effective diagnostic of these fluctuations in the presence of strongly inhomogeneous emissivity and large-scale velocity gradients. In Orion, the ordered large scale expansion of the nebula is an asymmetrical champagne flow away from the background molecular cloud (Zuckerman 1973), which produces systematically larger blue-shifts with increasing ionization (e.g., Fig. 11 of Baldwin et al. 2000). This offers a simple method for estimating the relative contribution of ordered versus turbulent motions to the total velocity dispersion. The mean systematic difference between the [O I] and [O III] centroid velocities is $\delta u = 9.4$ km s^{-1} (Table 2 of García-Díaz et al. 2008), which gives a champagne-flow contribution to the velocity dispersion of $\sigma_{\text{cham}} \approx 0.5\,\delta u = 4.7$ km s^{-1}. The turbulent contribution to the velocity dispersion is then $\sigma_{\text{turb}} \approx (\sigma_{\text{los}}^2 - \sigma_{\text{cham}}^2)^{1/2} = 3.7$ km s^{-1}. The uncertainties in this analysis are large, so that all that can be confidently asserted is that the ordered and turbulent velocity dispersions are roughly equal with $\sigma_{\text{cham}} \sim \sigma_{\text{turb}} = 4$–$5$ km s^{-1}.

APPENDIX A: PLANE-OF-SKY VERSUS LINE-OF-SIGHT VARIATIONS IN VELOCITY FROM SIMULATED H II REGION

For two representative times, Figure A1 shows the joint distribution of mean velocity $\bar{u}$ and non-thermal line width σ_{los}, calculated from the line profiles of synthetic position-position-velocity cubes for the simulated turbulent H II region of Medina et al. (2014). Figure A2 shows the temporal evolution of the plane-of-sky average and standard deviation of the same two quantities for the [O III] line. Results from the upper-right and lower-left panel of Figure A2 respectively provide the data that go into the horizontal and vertical axes of Figure 4(*b*) in § 4.3.

At late times (Fig. A1*c,d*), when dust absorption is relatively unimportant, the average line centroid velocity (upper left panel of Fig. A2) reflects the champagne flow due to the largest-scale density gradients in our simulation box. This leads to both blue and
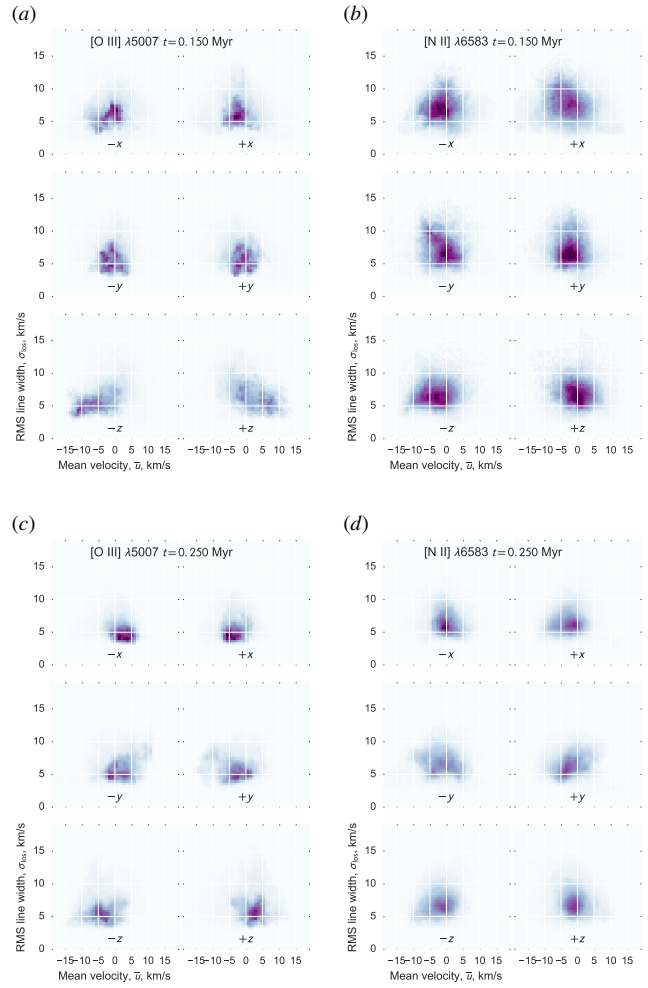

Figure A1. Joint probability densities of mean velocity $\bar{u}$ and line-of-sight velocity dispersion σ_{los} for two representative times in the evolution of a simulated H II region: 0.15 Myr (*a* and *b*) and 0.25 Myr (*c* and *d*). Line profile parameters are calculated for each position-position pixel of a synthetic position-position-velocity cube of the [O III] line (*a* and *c*) and [N II] line (*b* and *d*), which takes into account dust absorption (but not scattering) and thermal broadening at the local temperature. In each subfigure, results are shown for six viewing directions that correspond to the positive and negative principal axes of the simulation cube. The average thermal velocity width is subtracted in quadrature in order to mimic the observational methodology for isolating the non-thermal contribution to σ_{los}.

red shifts, since opposite viewing directions (e.g., $+x$ and $-x$) have roughly equal but opposite mean velocities, so that pairs of PDFs in Fig. A1*c,d* are rough mirror images. At earlier times (Fig. A1*a,b*), radial expansion dominates and the dust optical depth is larger, which leads to selectively greater absorption of receding regions of the nebula. This produces predominantly blue-shifted mean velocities from all viewing directions.

REFERENCES

Baldwin J. A., Ferland G. J., Martin P. G., Corbin M. R., Cota S. A., Peterson B. M., Slettebak A., 1991, ApJ, 374, 580

Baldwin J. A., Verner E. M., Verner D. A., Ferland G. J., Martin P. G., Korista K. T., Rubin R. H., 2000, ApJS, 129, 229

Brunt C. M., Federrath C., Price D. J., 2010, MNRAS, 403, 1507
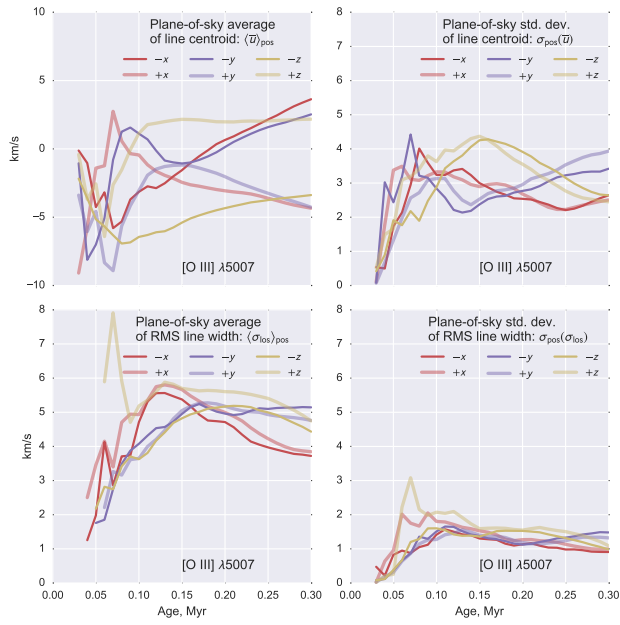
Figure A2. Temporal evolution of velocity statistics calculated from synthetic observed position-position-velocity cubes of the [O III] line, as illustrated in left panels of Fig. A2. Top row shows plane-of-sky average (left) and standard deviation (right) of the mean line velocity $\bar{u}$, while bottom row shows the same for the non-thermal RMS line width σ_{los}. Different colored lines correspond to viewing directions along each of the cube axes.

Castañeda H. O., 1988, ApJS, 67, 93

Deharveng L., 1973, A&A, 29, 341

García-Díaz M. T., Henney W. J., 2007, AJ, 133, 952

García-Díaz M. T., Henney W. J., López J. A., Doi T., 2008, Rev. Mexicana Astron. Astrofis., 44, 181

Henney W. J., 1998, ApJ, 503, 760

Medina S.-N. X., Arthur S. J., Henney W. J., Mellema G., Gazol A., 2014, MNRAS, 445, 1797

O'Dell C. R., 2001, ARA&A, 39, 99

Scalo J. M., 1984, ApJ, 277, 556

Tobin J. J., Hartmann L., Furesz G., Mateo M., Megeath S. T., 2009, ApJ, 697, 1103

von Hoerner S., 1951, ZAp, 30, 17

Zuckerman B., 1973, ApJ, 183, 863